Bulletin of the Seismological Society of America, Vol. 101, No. 3, pp. 1136–1151, June 2011, doi: 10.1785/0120100231

# Ground-Motion Simulations for the 1980 *M* 6.9 Irpinia Earthquake (Southern Italy) and Scenario Events

by Gabriele Ameri, Antonio Emolo, Francesca Pacor, and František Gallovič*

Abstract In this paper, we adopt three ground-motion simulation techniques (the stochastic finite-fault simulation code from Motazedian and Atkinson, 2005; the hybrid deterministic-stochastic approach with approximated Green's functions from Pacor *et al.*, 2005; and the broadband hybrid integral-composite technique with full-wavefield Green's functions from Gallovič and Brokešová, 2007), with the aim of investigating the different performances in near-fault strong-motion modeling and prediction from past and future events. The test case is the 1980 *M* 6.9 Irpinia earthquake, the strongest event recorded in Italy in the last 30 years. First, we simulate the recorded strong-motion data and validate the model parameters by computing spectral acceleration and peak amplitude residual distributions. The validated model is then used to investigate the influence of site effects and to compute synthetic ground motions around the fault. Afterward, we simulate the expected ground motions from scenario events on the Irpinia fault, varying the hypocenters, the rupture velocities, and the slip distributions. We compare the median ground motions and related standard deviations from all scenario events with empirical ground-motion prediction equations (GMPEs). The synthetic median values are included in the median $\pm$ 1 standard deviation of the considered GMPEs. Synthetic peak ground accelerations show median values smaller and with a faster decay with distance than the empirical ones. The synthetics total standard deviation is of the same order or smaller than the empirical one, and it shows considerable differences from one simulation technique to another. We decomposed the total standard deviation into its between-scenario and within-scenario components. The larger contribution to the total sigma comes from the latter, while the former is found to be smaller and in good agreement with empirical interevent variability.

*Online Material:* Comparison of observed and simulated waveforms and spectra.

## Introduction

One of the key steps of a seismic hazard assessment study is the prediction of ground-motion parameters, assuming the occurrence of specific earthquakes. This goal may be easily pursued using ground-motion prediction equations (GMPEs) that provide the probability distribution of earthquake ground motion at a given site as a function of, for example, magnitude, distance, site condition, and fault mechanism (Ambraseys *et al.*, 2005; Boore and Atkinson 2008; Bindi *et al.*, 2009; Akkar and Bommer, 2010; among many others). Although they are retrieved through the analysis of recorded strong-motion data, the GMPEs account only for the average characteristics of the earthquake source and wave-propagation processes. In general, at distances comparable with the fault dimensions, the complexity and heterogeneity of the source rupture process may strongly influence the ground motion, especially in the case of moderate-to-large earthquakes (Archuleta and Hartzell, 1981; Heaton, 1990). This feature is crudely accounted for by GMPEs, due to the simplistic source parameterization adopted in the functional forms, and to the paucity of strong-motion data recorded at near-source distances for large magnitudes. This is the case in Italy, where only a few strong-motion data recorded in the proximity of the rupturing fault are available, even in the case of moderate-to-large instrumental earthquakes (Luzi *et al.*, 2008; also see the Data and Resources section for information about the Italian Accelerometric Archive).

An alternative approach to predict earthquake ground motions is represented by the simulation of synthetic accelerograms through either purely stochastic or hybrid

*Also at Dipartimento di Scienze Fisiche, Università degli Studi "Federico II", Napoli, Italy.

deterministic-stochastic methods. These methods are able to generate realistic seismograms in the frequency band of engineering concern, close to the causative fault (e.g., Zollo *et al.*, 1997; Mai and Beroza, 2003; Motazedian and Atkinson, 2005; Pacor *et al.*, 2005; Gallovič and Brokešová, 2007;) and can be used to perform earthquake scenarios studies (Aagaard *et al.*, 2008; Ameri *et al.*, 2008; Cultrera *et al.*, 2010). However, these methods are generally considered as advanced tools in hazard assessment framework, because compared with GMPEs, they require a larger number of seismological data about the earthquake source and the propagation medium, which are often uncertain.

The most widely used simulation techniques are based on a kinematic model of the extended source and require the specification of parameters describing the rupture evolution (slip function, rupture velocity, nucleation point position, etc.). These parameters have to be sought when one is interested in reproducing strong-motion records associated with an occurred earthquake (Mena *et al.*, 2006; Ameri *et al.*, 2009). On the contrary, when seismic hazard studies and earthquake scenarios are carried out, the parameters describing the rupture evolution need to be varied in order to produce a large number of scenario events. This approach is supported by the fact that it is not possible to predict which rupture scenario will occur on a seismogenic fault. In this way, various possible rupture processes, occurring on the same fault, are simulated and for each of them, synthetic seismograms are computed. The required strong-motion parameters at the site of interest are then expressed through a statistical analysis of the simulated seismograms (Convertito *et al.*, 2006; Emolo *et al.*, 2008; Cultrera *et al.*, 2010; Chiauzzi *et al.*, 2010), and the associated variability may be studied and quantified (Ripperger *et al.*, 2008).

The approximations introduced in the numerical representation of the rupture and wave-propagation processes entail, however, that the ground motion simulated at a given site by different techniques is generally different in some features (e.g., signal duration, peak values in specific frequency ranges, etc.). As a consequence, some techniques are not able to reproduce specific ground-motion characteristics as, for example, directivity pulses or polarization of ground motion.

Furthermore, synthetic seismograms should be validated in some way, in order to demonstrate the reliability of the ground-motion estimates. Some examples can be found in Convertito *et al.* (2006), Sørensen *et al.* (2007), Gallovič and Burjánek (2007), Gallovič and Brokešová (2007), Ansal *et al.* (2008), Ameri *et al.* (2008), Emolo *et al.* (2008), Cultrera *et al.* (2009), and Graves and Pitarka (2010).

In this paper, we apply three finite-fault simulation techniques to reproduce the ground motion during the 1980 *M* 6.9 Irpinia (southern Italy) earthquake and generate scenario events. The aim is to investigate the different performances of the simulation techniques in near-fault strong-motion modeling and prediction from past and future events. First, we synthesize accelerometric records at some of the near-fault sites that recorded the Irpinia earthquake and evaluate the capability of the simulation methods to reproduce the main features (amplitude and frequency content) of observed strong-motion data. Then we compute synthetic accelerograms at a dense grid of virtual observers, simulating a large number of possible scenario events. We produce, for each simulation technique, synthetic data sets that we treat statistically in order to evaluate the median ground motion and the associated variability. In particular, similar to what is done in the framework of the GMPEs (e.g., Atik *et al.*, 2010), we separate the total variability in the interscenario (between-scenario) and intrascenario (within-scenario) components. The interscenario component measures the variability among the average ground motions predicted by all scenario events, and the intrascenario variability measures the variability of the ground motion with respect to the average motion predicted for each earthquake scenario.

## Simulation Methods

In this work we use three well-known simulation methods: the stochastic finite-fault simulation code (EXSIM, Motazedian and Atkinson, 2005; Boore, 2009), the hybrid deterministic-stochastic approach with approximated Green's functions (DSM, Pacor *et al.*, 2005), and the broadband hybrid integral-composite technique with full-wavefield Green's functions (HIC, Gallovič and Brokešová, 2007). Table 1 summarizes the main characteristics of each technique in terms of source and path parameters; Table 2 reports the input modeling parameters later described. Here, we recall some key elements about the source representation for each technique and refer, for further explanation, to the previously mentioned reference papers.

The EXSIM and DSM techniques are both an extension of the point-source stochastic method (Boore, 1983, 2003) to include the rupture propagation along an extended fault. The kinematic rupture model is simply described assigning the slip distribution, the rupture velocity, and the nucleation point on the fault. In EXSIM, the fault is divided into $N$ subfaults; each of them is considered as a point source, emitting an $\omega$-square spectrum. Ground motions produced by subfaults are summed in the time domain, with a proper time delay, to obtain the ground motion from the entire fault. The DSM generates acceleration envelopes using the isochrone theory (Bernard and Madariaga, 1984; Spudich and Frazer, 1984). For a given site, each instant of time of the envelope is constructed by summing the contributions to ground motion from the corresponding isochrone on the fault. The spectral content of the synthetic seismogram is then defined through a reference spectrum. This spectrum corresponds to an $\omega$-square model, with fixed corner frequency (hereafter referred to as $\mathrm{DSM_{fix}}$) or with apparent corner frequency (hereafter referred to as $\mathrm{DSM_{app}}$), given by the inverse of the envelope duration, different from site to site. In this latter case the directivity-induced amplification effect on the ground motion related to the rupture

Table 1
Source and Wave-Propagation Processes as Modeled in the Considered Simulation Methods

| Method | Source | Path |
|---|---|---|
| **EXSIM** (Motazedian and Atkinson, 2005; Boore, 2009) | The fault is divided into $N$ subfaults; each of them is considered as a point source radiating an $\omega^2$ spectrum. Ground motions produced by subfaults are summed in the time domain, with a proper time delay, depending on the rupture time distribution, to obtain the ground motion from the entire fault.<br>The slip distribution and a constant rupture velocity can be specified. | Stochastic Green's functions: homogenous medium ($V_S$ is specified at the source).<br>Spectral attenuation is defined by geometrical spreading + quality factor + kappa.<br>Frequency-dependent crustal amplification function, to account for wave amplification through the layered model.<br>Distance-dependent duration of seismograms. |
| **DSM** (Pacor *et al.*, 2005; Ameri *et al.*, 2009) | An acceleration envelope is computed by the isochrone theory at any given site: the duration is defined by rupture propagation + crustal propagation. The envelope amplitude is modulated for the slip distributions on the fault. The deterministic envelope is then used to window a white noise time series and multiplied by an $\omega^2$ reference spectrum. The finite-fault characteristics such as distance, radiation pattern and corner frequency (either apparent or fixed) are parameters of the spectrum. | Semistochastic Green's functions: Deterministic envelopes (duration and shape) defined through isochrones for a 1D layered medium.<br>Spectral attenuation is defined by geometrical spreading + quality factor + kappa.<br>Frequency-dependent crustal amplification function, to account for wave amplification through the layered model. |
| **HIC** (Gallovič and Brokešová, 2007) | The rupture process at the seismic source is described in terms of slipping of elementary subsources with fractal number-size distribution (fractal dimension 2), randomly placed on the fault plane.<br>At low frequencies: based on the representation theorem assuming a final slip distribution composed from the subsources, which is characterized by a $k$-squared decay. At high frequency, instead, the ground-motion synthesis is obtained summing the contributions from each individual subsource treated as a point source. Low- and high-frequency synthetics are combined in the frequency domain. | Full-wavefield Green's functions by DWN technique.<br>Spectral attenuation is defined by quality factor + kappa |

Table 2
Parameters Used in the Simulation of the Irpinia 0 s and of the Scenario Events*

| Parameter | Irpinia Earthquake (0 s event) | Method |
|---|---|---|
| Fault mechanism† | Strike: 315°, dip: 60°, rake: −90° | 1,2,3 |
| Fault dimensions | Length 35 km, width 15 km | 1,2,3 |
| Fault top depth | 2.2 km | 1,2,3 |
| Focal depth | 10.9 km | 1,2,3 |
| Seismic moment | $2 \times 10^{19}$ N m | 1,2,3 |
| Shear-wave velocity, $V_S$ | 3.2 km/s | 1,2 |
| Density, $\rho$ | 2.9 g/cm$^3$ | 1,2 |
| Radiation pattern | 0.55 | 1,2 |
| Number of subfaults | Along strike 70; along dip 30 | 1,2,3 |
| Slip distribution‡ | #1 | 1,2,3 |
| Nucleation point‡ (position from southeast edge) | Down-dip 10 km; along strike 5 km | 1,2,3 |
| Rupture velocity ($V_r$)‡ | $0.8V_S$ | 1,2,3 |
| Stress parameter ($\Delta\sigma$)‡ | 80 bars | 1,2 |
| $k$ | 0.03 s | 1,2,3 |
| Quality factor | 100 | 1,2 |
| Geometrical spreading | $1/R$ | 1,2 |
| Distance-dependence duration§ | $T_0 + 0.05R$ ($R > 10$ km) | 1 |
| Crossover frequency | 0.5–2.0 Hz | 3 |
| Number of simulations | 40 | 1,2 |

*The parameter required by each method is specified in the Method column (1, EXSIM; 2, DSM; 3, HIC).
†In the HIC method, random variations within ±30° from the adopted values are prescribed for the high-frequency subsources.
‡These parameters are changed in the scenario-events simulations; see the main text for details.
§Where $T_0$ is the subfault source duration defined as $1/f_{0sf}$ ($f_{0sf}$ is the subfault corner frequency).

propagation along the extended fault is included in the $\omega$-square spectrum by the apparent corner frequency.

The HIC technique simulates the rupture process in terms of slipping of elementary subsources with fractal number-size distribution (fractal dimension 2), randomly placed on the fault plane (Zeng *et al.*, 1994). At low frequencies, the source description is based on the representation theorem (integral approach, Aki and Richards, 2002), assuming a final slip distribution composed from the subsources, which is characterized by a $k$-squared decay (Herrero and Bernard, 1994; Gallovič and Brokešová, 2004). At high frequency, instead, the ground-motion synthesis is obtained summing the contributions from each individual subsource treated as a point source (composite approach). The Green's functions for both frequency bands are evaluated by the discrete wavenumber technique (Bouchon, 1981) in a layered 1D medium.

## The 23 November 1980 *M* 6.9 Irpinia Earthquake

The Irpinia earthquake (southern Italy) is the largest event recorded by strong-motion instruments in Italy. The earthquake was widely studied and a complete review was published in a special issue of *Annals of Geophysics* (vol. 36, n. 1, 1993). It was a normal-faulting complex event that involved at least three distinct shocks starting in a time span of approximately 40 s (Fig. 1): the main event (further referred to as the 0 s event) was followed by two further rupture episodes delayed about 20 s and 40 s, respectively (Bernard and Zollo, 1989; Pantosti and Valensise, 1990). The characteristics of the 0 s event have been deeply investigated (Cocco and Pacor, 1993; Giardini, 1993; Pingue *et al.*, 1993); this shock was related to the rupture of a normal fault striking in the Apennine direction and dipping 60° toward the northeast (Table 2).

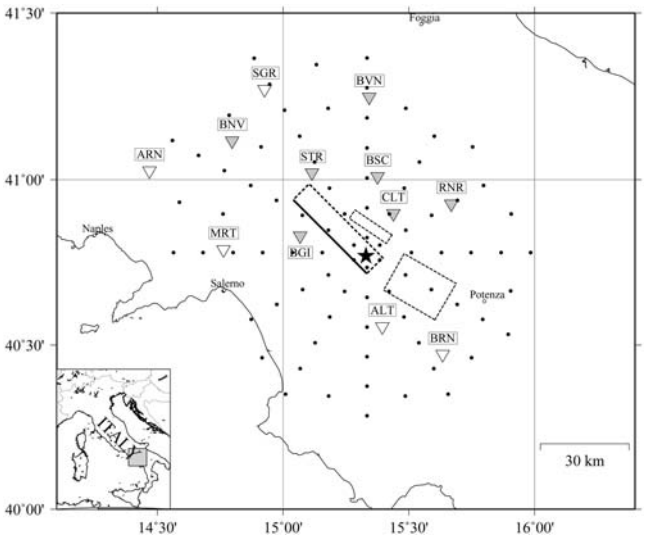


**Figure 1.** Geometry of the three fault segments whose rupture caused the 1980 Irpinia earthquake. The epicenter of the 0 s fault segment is shown by the black star; the fault top is shown by the thick black line. The 10 stations belonging to the Italian strong-motion network within 60 km of the epicenter are represented as triangles (see Table 1 for the station code). Filled triangles highlight the 7 stations that have been used in the strong-motion modeling performed in this study. Black dots indicate the 86 virtual receivers used in the scenario-events simulations. The virtual receivers are within 50 km of the fault surface projection.

The earthquake triggered 21 analog accelerometric stations, 10 of them at epicentral distances within 60 km (Fig. 1). The near-fault strong-motion records are characterized by a very long duration, about 80 s, and the three events can be clearly detected with the exception of the southernmost stations, BRN and ALT, which were likely triggered by the 20 s event. The recording stations in the epicentral area are classified mostly as rock and stiff sites. All information related to their geological and geotechnical characteristics are taken from the corresponding monographs recently published in the Italian strong-motion database (ITACA; see the Data and Resources section).

We selected seven near-fault stations that clearly recorded the 0 s event and are weakly affected by site effects (Table 3). The maximum peak ground acceleration (PGA) and peak ground velocity (PGV) values (3.01 m/s$^2$ and 0.70 m/s, respectively) were recorded at STR on the east–west component. These high peak ground motions may be ascribed to directivity effects related to the position of the site with respect to the direction of the rupture propagation on the 0 s fault (Cultrera *et al.*, 2010).

A rough estimation of the frequency content of the records may be inferred by the PGA/PGV ratio (Kwon and Elnashai, 2006), which is equal to $0.58 \pm 0.11\ g/\mathrm{ms}^{-1}$, considering the mean ratio for data in Table 3. Following the classification by Zhu *et al.* (1988) and Kwon and Elnashai (2006), the 1980 Irpinia near-fault ground motions can be classified as high velocity–low acceleration (HV–LA) records. Low PGA/PGV ratios signify earthquakes with low predominant frequencies, broader response spectra, and longer duration (Kwon and Elnashai, 2006). Other earthquakes in different tectonic environments (e.g., the $M_w$ 7.4 1999 Chi-Chi earthquake) show similar HV–LA behavior.

### Source and Propagation Models

In this work we used the fault geometry and 1D crustal model (Tables 2 and 4) as described by Cultrera *et al.* (2010), that simulated seismic scenarios from different rupture models of the 0 s fault, in order to study the source-related variability of low-frequency ground motions. The kinematic rupture model considered for the 0 s fault is based on the study of Cocco and Pacor (1993): the final slip distribution is characterized by two main asperities, the largest located close to the southern edge of the fault and the other located close to the northern edge, both at a depth between 6.5 and 11 km. Starting from the slip and rupture time distributions originally proposed by the authors, we calculated a $k^{-2}$ slip model (Herrero and Bernard, 1994; Gallovič and Brokešová, 2004) shown in Figure 2a. The position of the nucleation

Table 3
Selected Accelerometric Stations and Relative Ground-Motion Parameters Recorded

| Station | Code | $R_{epi}$* (km) | $R_{JB}$† (km) | $PGA_{max\,H}$ (m/s$^2$) | $PGV_{max\,H}$ (m/s) | PGA/PGV ($g$/ms$^{-1}$) | EC8 class‡ |
|---|---|---|---|---|---|---|---|
| Bagnoli | BGI | 22 | 7 | 1.83 | 0.35 | 0.54 | B |
| Benevento | BNV | 58 | 28 | 0.58 | 0.09 | 0.64 | B |
| Bisaccia | BSC | 28 | 18 | 0.95 | 0.22 | 0.45 | A |
| Bovino | BVN | 54 | 35 | 0.47 | 0.06 | 0.75 | B |
| Calitri | CLT | 19 | 13 | 1.72 | 0.29 | 0.59 | B |
| Rionero | RNR | 36 | 29 | 0.97 | 0.15 | 0.66 | B |
| Sturno | STR | 33 | 4 | 3.10 | 0.70 | 0.45 | B |

*Calculated from the 1980 Irpinia earthquake epicenter (41.76° N, 15.31° E).

†The $R_{JB}$ is the distance from the surface projection of the fault as introduced by Joyner and Boore (1981). The $R_{JB}$ distance has been computed with respect to the 0 s fault.

‡The sites were classified according to the Eurocode 8 (CEN, Comité Européen de Normalisation, 2004) and the Italian Building Code (NTC08, Norme Tecniche per le Costruzioni, 2008), based on the shear-wave velocity averaged over the top 30 m of the soil profile ($V_{S30}$). The EC8 classes are the following: class A, $V_{S30} > 800$ m/s; class B, $V_{S30} = 360$–$800$ m/s; class C, $V_{S30} = 180$–$360$ m/s; class D, $V_{S30} < 180$ m/s; class E, 5 to 20 m of C- or D-type alluvium underlain by stiffer material with $V_S > 800$ m/s.

point (largest star in Fig. 2a) corresponds to the instrumental epicenter (40.76° N, 15.31° E); the rupture velocity was set at $0.8V_S$, where $V_S$ is the shear-wave velocity (see Table 4).

The spectral attenuation was defined in terms of quality factor $Q$ and high-frequency decay parameter $\kappa$ (Anderson and Hough, 1984). The depth-dependent $Q_p$ and $Q_s$ values used for HIC simulations are reported in Table 4. In DSM and EXSIM, a $Q_S = 100$ was adopted in order to obtain results comparable with HIC simulations and as reported by Cultrera *et al.* (2010). We set $\kappa = 0.03$ s, according to literature estimates for rock and stiff sites (Margaris and Boore, 1998; Bindi *et al.*, 2004).

A crustal amplification function has been used in EXSIM and DSM simulation techniques to account for frequency-dependent amplification of seismic waves through the *S*-waves velocity profile of the crustal model (Boore and Joyner, 1997). For the Irpinia area, we adopted an amplification function for hard-rock sites (Siddiqqi and Atkinson, 2002; Atkinson and Boore, 2006), characterized by a shear-wave velocity near the surface of about 2000 m/s (class A according to the National Earthquake Hazards Reduction Program, 1994), which is comparable to the velocity we used (Table 4).

The value of the stress parameter $\Delta\sigma$ has been set to 80 bars on the basis of a trial-and-error analysis performed through the comparison of observed and synthetic high-frequency level of the Fourier amplitude spectra (S3 Project Deliverable D0, 2007).

The input parameters for the three techniques adopted to simulate the 0 s events are summarized in Table 2.

## Modeling of the Strong-Motion Data

We calculated the synthetic seismograms at the selected stations using the three simulation techniques and adopting the source and propagation models described previously (Tables 2 and 4). The comparisons with the recorded data, in terms of acceleration and velocity waveforms (north–south and east–west components) and spectral acceleration (SA) in the frequency band 0.1–12 Hz, are reported in Ⓔ Figures S1 to S6 in the electronic supplement to this paper. Here, for example, we show the results for the HIC technique (Fig. 3). The HIC synthetics are the most suitable to discuss the goodness of the adopted rupture and propagation models because this approach adopts complete Green's functions and solves deterministically the representation theorem at low frequencies.

For most of the sites, the simulated time series are in good agreement with the recorded ones, both in time and frequency domains. The good fit for BGI station, located just a few kilometers from the fault, supports the reliability of the

Table 4
Velocity Model Used in This Simulation Study*

| Depth (km) | $V_P$ (km/s) | $V_S = v_P/1.81$ (km/s) | Density (g/cm$^3$) | $Q_P$ | $Q_S$ |
|---|---|---|---|---|---|
| 0 | 3.5 | 1.93 | 2.3 | 200 | 100 |
| 2 | 4.5 | 2.49 | 2.5 | 300 | 150 |
| 4 | 5.7 | 3.15 | 2.6 | 500 | 200 |
| 10 | 6.5 | 3.59 | 2.7 | 750 | 250 |
| 25 | 7.5 | 4.14 | 2.9 | 900 | 300 |
| 35 | 8.1 | 4.48 | 3.2 | 1200 | 400 |

*This model is based on data from L. Improta (personal commun., 2007), and also loosely based on data from Amato and Selvaggi (1993) and Improta *et al.* (2003).

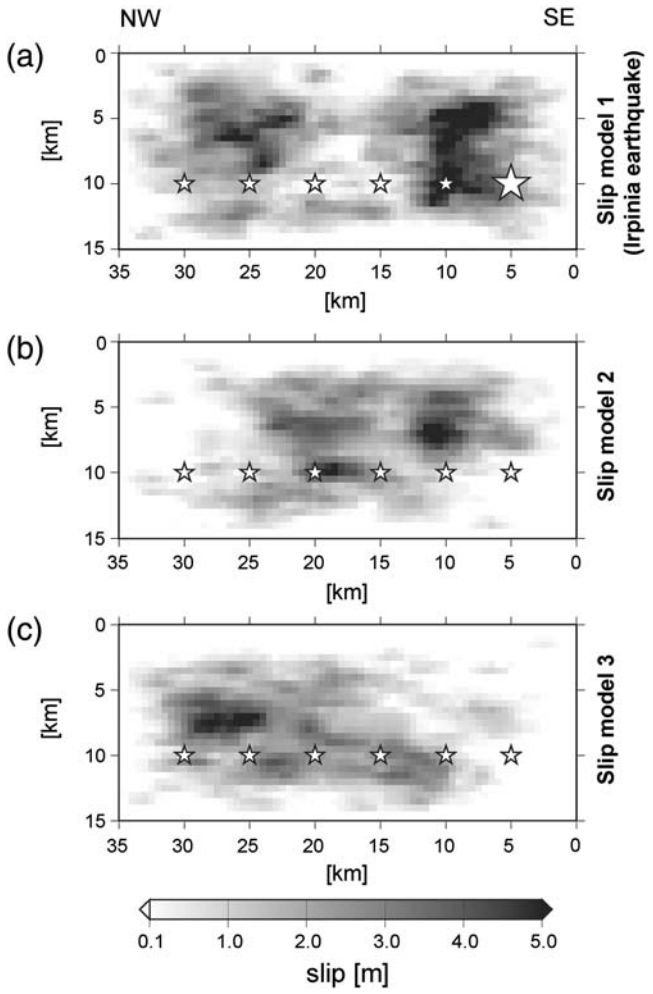


**Figure 2.** *K*-squared slip distributions and hypocenter locations (white stars) used in the simulations. Slip model in the top panel mimic the one inferred by Cocco and Pacor (1993), characterized by two main asperities, the largest located close to the southern edge of the fault and the other to the northern edge. This slip is used to model the Irpinia 1980 earthquake ground motions. The largest star represents instrumental hypocenter (40.76° N, 15.31° E). The fault plane is discretized into $70 \times 30$ subfaults.

adopted rupture model. Also the waveforms at the farthest stations, BVN and BNV, located about 30 km from the fault, are well simulated, indicating that the 1D propagation model accounts for the main observed phases. BSC synthetics spectra well reproduce the observed ones at frequencies larger than 1 Hz. The misfit at lower frequencies (around 0.5 Hz) is likely due to the velocity inversion in the soil profile below the station (Olivares and Silvestri, 2001; Cultrera *et al.*, 2010), not accounted for in the simulations.

A worse fit is obtained for CLT, RNR, and STR, where the observed ground motion is underestimated. Indeed, at CLT, the HIC synthetics are not able to simulate the large amplitude of the later arrivals, while at RNR the waveforms are deficient of high-frequency energy. Finally at STR, less than 5 km from the fault, we are only able to fit the first large phases of the north–south component. The lower ground-motion amplitude simulated in the east–west direction can be ascribed to the effect of the radiation pattern. This is not observed in the records, likely due to the small-scale variations of the source mechanism, not included in the model.

Regarding the other two simulation techniques (Ⓔ Figures S2, S3, S5 and S6, available as an electronic supplement to this paper), the use of simplified Green's functions does not allow us to reproduce correctly the phases of the observed seismograms. The spectral content and peak amplitudes are well reproduced at BGI and BSC and, similar to HIC, they are underestimated at RNR, CLT, and STR.

To summarize the modeling results and to assess the performance of the simulation techniques, we computed the SA, PGA, and PGV residuals ($\log_{10}$[observed/simulated]) at each station. Spectral acceleration residuals at each frequency are then averaged over the seven stations, yielding a measure of the model bias (Fig. 4). In general, the simulations provide small model biases, with a tendency to positive values (i.e., average underestimation) over the entire frequency range. This result is expected because the synthetics are simulated at bedrock, while the recording sites, although located on stiff soils, are characterized by variable local geology. Nevertheless, the models' biases do not exceed 0.25, which means an average underestimation of less than a factor of 2. HIC residuals are less scattered at low frequencies ($< 1$ Hz), while EXSIM and DSM have a similar $\sigma_{\text{bias}}$ (i.e., similar scatter of the residuals), with a tendency to lower sigma in the intermediate frequency range ($\sigma_{\text{bias}} \approx 0.15$) and higher values at both low and high frequencies ($\sigma_{\text{bias}} \approx 0.25$). The positive and negative residuals outside the standard deviation are related to RNR, CLT, and STR sites, as already noted in Figure 3.

Possible site amplification at these stations are evaluated computing the horizontal-to-vertical spectral ratios (HVSR) (Lermo and Chávez-García, 1993), using all the strong-motion data available (Fig. 5). RNR, located on volcanic rocks, shows flat HVSR, while small broadband amplifications are obtained at CLT and STR, installed on silty clays and weathered sandstone, respectively. Note that the paucity of strong-motion data at RNR (three records), together with possible amplification on the vertical component, may lead to unreliable HVSR results.

The STR and CLT HVSR mean amplification curves are used to multiply the Fourier amplitude spectra of the synthetics computed at bedrock, maintaining the phases unchanged. The geometric mean acceleration response spectra of amplified synthetic time series are shown in Figure 6. In general, the fit improves, with the exception of HIC results at CLT. In this case an overestimation of the high-frequency content ($f > 2$ Hz) is observed; further investigations may be carried out to explain the role of the site response at this station.

In conclusion, due to the relatively small number of records considered, it is difficult to establish which method performs better in the modeling of the 1980 earthquake strong-motion data. We note a general consistency among the simulation results in terms of spectral accelerations and

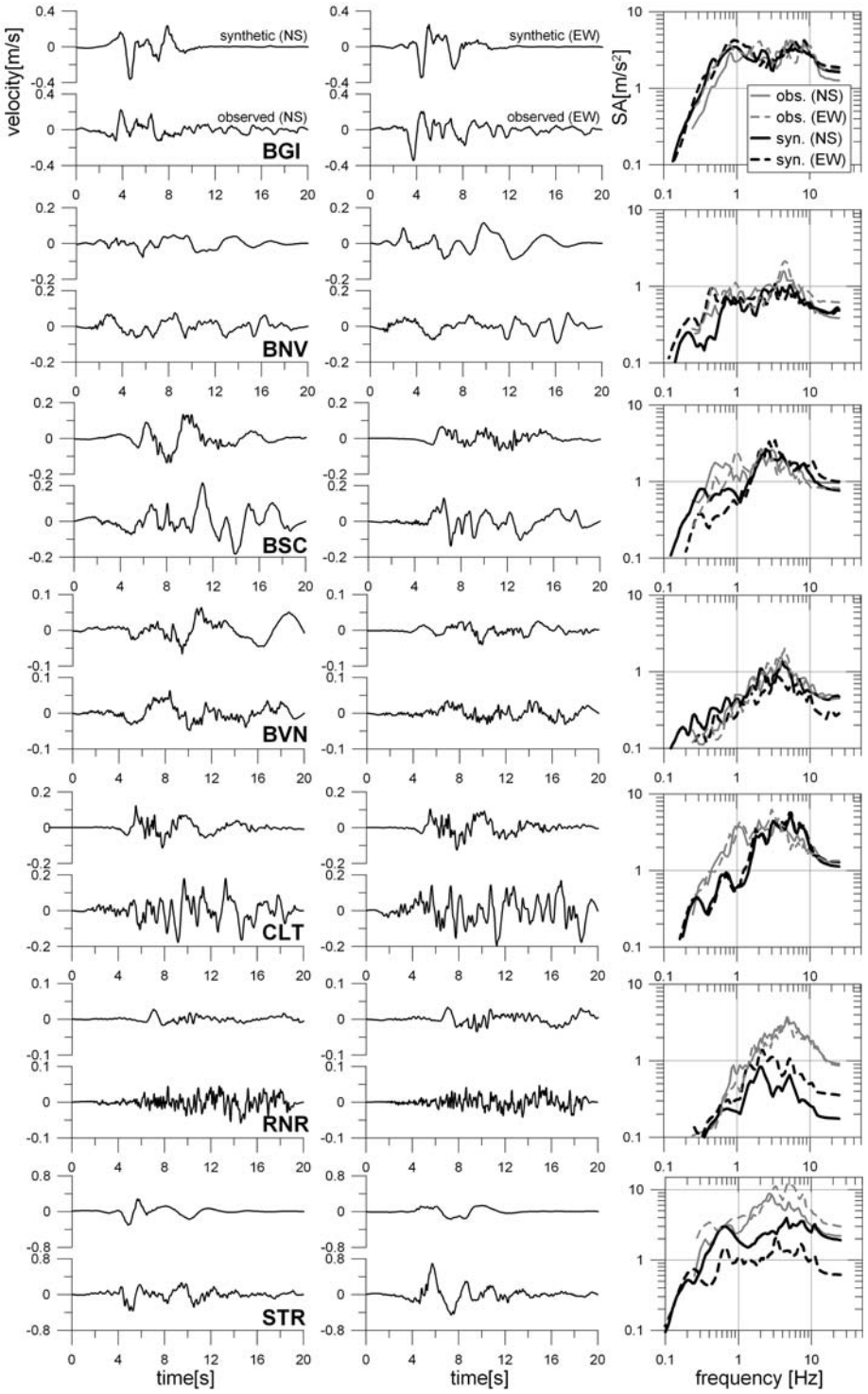


**Figure 3.** Comparison of north–south (NS) and east–west (EW) recorded and simulated velocity time series at the 7 selected stations (see Fig. 1) considering the HIC technique. The right panels show the comparison in terms of spectral accelerations (SA) at 5% damping. Time series have been filtered between 0.1 and 12 Hz, and the first 20 s of signal have been considered. Ⓔ See Figure S1 in the electronic supplement to this paper for a comparison of acceleration waveforms.

peak values, whereas the synthetic waveforms show notable differences in duration and phase. Moreover, the effect of local site amplification seems unimportant at the considered stations, except at RNR, where we are not able to explain the high-frequency content of the observed waveforms with the adopted source, propagation, and site parameters. Overall, the results presented in Figures 3 and 4 make us confident that the methods can be used to predict the bedrock ground motion associated to the 1980 and other scenario events for the study area.

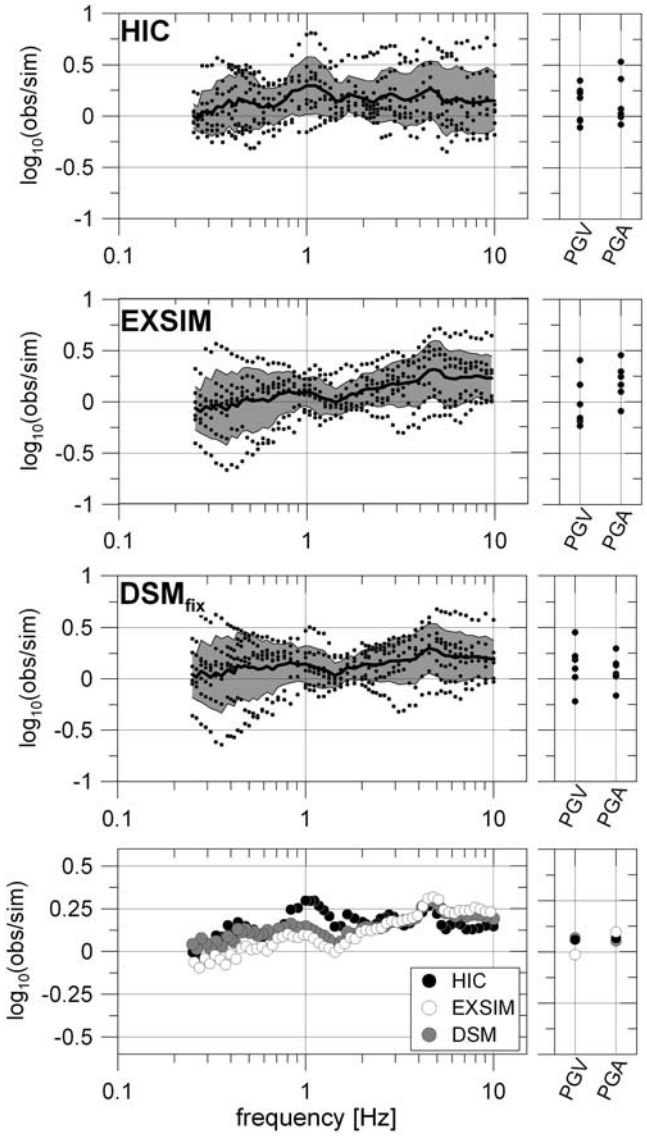


**Figure 4.** Spectral accelerations, PGV, and PGA residuals (black dots), defined as the $\log_{10}$(observed/simulated), considering the geometric mean of NS and EW components are shown for the three simulation techniques. Spectral acceleration residuals are computed for 17 frequencies ranging from 0.25 to 10 Hz. The model bias (black line), defined as the mean of the residuals at each frequency, and relative standard deviation (gray shaded area) are also shown. The bottom panel shows a comparison among the model biases computed with the three simulation techniques.

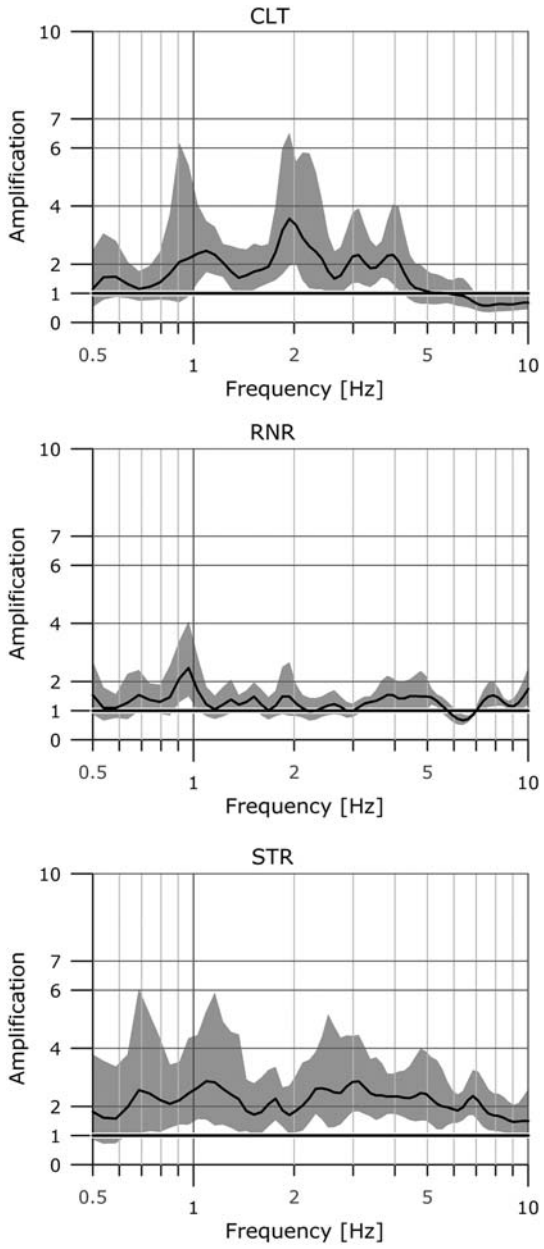


**Figure 5.** HVSR mean curves (black continuous lines) plus/minus one standard deviation (shaded area) computed for CLT, RNR, and STR stations using 6, 3, and 9 records, respectively. The analysis was performed on the *S*-wave windows selected starting about 1 s before the *S*-wave onset and ending when 90% of the total energy of the signal has been released, assuming that this interval corresponds to the strong-motion phase.

## Ground-Motion Scenario

The validated model is used to simulate the ground motion for the 0 s event at a dense grid of 86 virtual receivers (their positions are shown in Fig. 1), in order to evaluate the spatial distribution of the ground motion predicted by the three methods. The PGA and PGV maps computed for bedrock sites are shown in Figure 7. For all the simulation techniques, the finite dimension of the fault produces contour lines slightly elongated in the fault-strike direction. Moreover, the ground motion decays more slowly in the northwestern direction, that is, in the direction toward which the rupture propagates rather than in the opposite direction.

The PGA maps simulated with $DSM_{fix}$, EXSIM, and HIC techniques show an almost isotropic distribution with respect to the fault projection, because similar approaches are implemented in modeling the high-frequency component of the radiation emitted by the extended source. For instance, in the HIC technique, the high-frequency content is simulated through an incoherent sum of the energy emitted by the

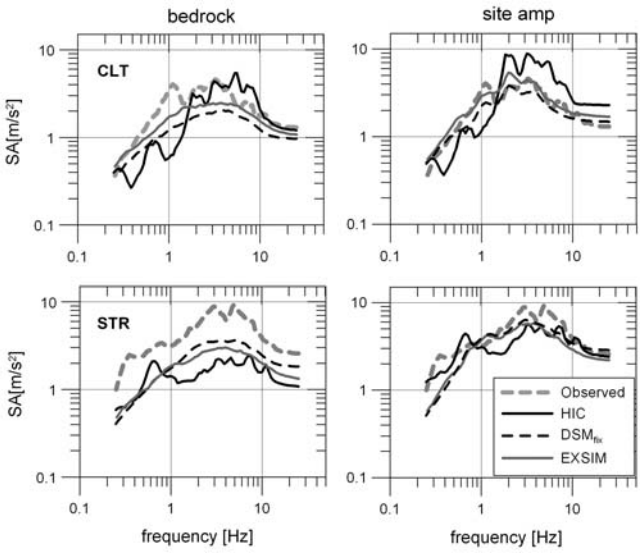


**Figure 6.** Comparison of simulated and observed spectral accelerations (SA, at 5% damping), geometric mean of north–south and east–west components, at CLT and STR stations. Left plots: simulations are performed at bedrock. Right plots: site amplification is accounted in the simulations by HVSR-based amplification functions (Fig. 5). DSM and EXSIM response spectra are geometric mean of the 40 realizations.

stochastic elementary subsources (composite approach), resulting rather independently from the source-to-receiver azimuth (see also Gallovič and Burjanek, 2007). On the other hand, the rupture directivity effects on the ground motion are evident in the HIC PGV map, where the area of maximum is shifted far from the epicenter and close to the BGI and STR stations. This is caused by the deterministic calculation of ground motion at low frequencies (mostly affecting the PGV), preserving the inherent directivity effect. In particular, the large PGV area in Figure 7a is due to the combined effect of the northwestern and up-dip rupture propagation, position of the second asperity (Fig. 2a), and radiation pattern.

We also showed in Figure 7d the maps generated with $DSM_{app}$ in order to evaluate the influence of the apparent corner-frequency approach on the spatial distribution of ground motion. The peak ground motions strongly change with respect to $DSM_{fix}$, predicting large amplitudes close to the northwestern edge of the fault, thus modeling the effect of rupture directivity on both the simulated PGA and PGV. The difference between the $DSM_{fix}$ and $DSM_{app}$ predictions is due to the use of different corner frequencies in the source spectrum. In the first case, following the classical $\omega$-square model, the corner frequency is defined as $f_c = 4.9\times 10^6 V_S(\Delta\sigma/M_0)^{1/3}$, assuming a fixed value for all sites. In the second case, the corner frequency is calculated as the inverse of the source duration as perceived at each site (i.e., the apparent corner frequency). For example, a corner frequency $f_c = 0.11$ Hz is obtained adopting $\Delta\sigma = 80$ bar. On the other hand, the apparent corner frequencies obtained at STR and CLT sites are $f_a = 0.16$ Hz and $f_a = 0.05$ Hz, respectively. Because the high-frequency plateau of the acceleration source spectrum in the $\omega$-square model is proportional to $M_0 f_c^2$, it is clear that the two approaches can lead to very different simulated ground motions.

Although based on different approaches, $DSM_{app}$ and HIC generate consistent PGV distributions. On the other hand, $DSM_{app}$ generates high PGA values close to the STR station and small values at sites located in the opposite direction (e.g., RNR and CLT). Such large differences are, however, not observed in the records, suggesting that $DSM_{app}$ might overemphasize the forward and backward directivity effects close to the fault.

To verify the reliability of the ground-motion scenario for the 0 s event, the synthetic PGA and PGV values are compared with predictions from Akkar and Bommer (2010, hereafter referred to as AkB10) GMPEs (Fig. 7, right panels).

For the three simulation techniques, the synthetic PGAs underestimate the empirical median prediction and show a stronger attenuation with distance, while the PGVs match the median values well over the considered distance range. Overall, the recorded peaks are better fitted by the synthetics both for acceleration and velocity.

The HIC PGV and $DSM_{app}$ PGA and PGV values as a function of distance are largely scattered, and some values are outside of the AkB10 standard deviation. This scatter is caused by the concurrent presence, at similar $R_{JB}$ distances, of receivers that experience both forward and backward directivity.

The ground-motion scenarios for the 0 s event show PGA that are, on average, smaller and decay faster with distance than the average predictions from the considered GMPE, confirming the HV–LA property observed from the Irpinia earthquake records. The average simulated PGA/PGV ratios are $0.71 \pm 0.50$ $g/\mathrm{ms}^{-1}$ for HIC, $0.49 \pm 0.12$ $g/\mathrm{ms}^{-1}$ for EXSIM, $0.60 \pm 0.16$ $g/\mathrm{ms}^{-1}$ for $DSM_{fix}$, and $0.57\pm 0.15$ $g/\mathrm{ms}^{-1}$ for $DSM_{app}$.

## Ground-Motion Prediction for $M_w$ 6.9 Scenario Events

The next step of this study is the generation of ground-motion scenarios at bedrock, associated with a fault having the geometry, orientation, and seismic moment of the 0 s fault in order to characterize the potential variability in ground motions for future events of this size on the Irpinia fault. The variability related to the local site response is not included in this analysis.

A similar study was performed by Cultrera *et al.* (2010) using a discrete-wavenumber/finite-element technique with the aim of investigating the low-frequency parametric variability of the ground motion (up to 2 Hz) as a function of different source parameters (i.e., rupture velocity, slip distribution, nucleation point, and source time function). They showed how the distributions of spectral displacement at 2 s and of PGV depend on both azimuth and distance and how the simulated ground motion is influenced by the source parameters. In this study we extend the scenario-events

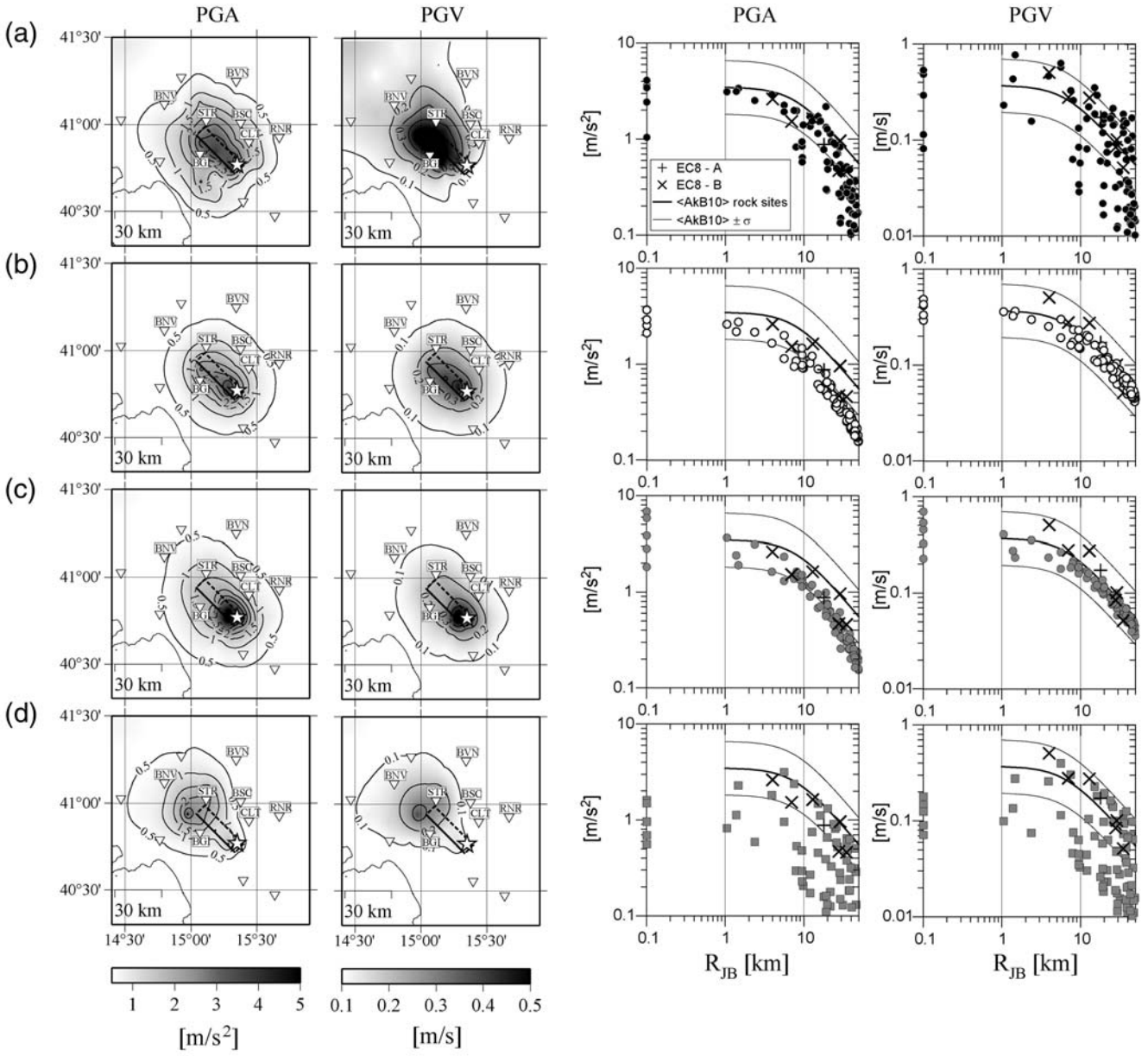


**Figure 7.** PGA and PGV values (geometric mean of north–south and east–west components) for the Irpinia earthquake rupture scenario simulated with HIC (a), EXSIM (b), $DSM_{fix}$ (c), and $DSM_{app}$ (d) techniques. Left columns show the map distribution of peak values and right columns their decay as a function of $R_{JB}$. The values are simulated at virtual grid points shown in Figure 1. Peak values recorded during the 1980 Irpinia earthquake (classified according to EC8 site classification) are also shown (right columns). The black curves in the right columns represent the median peak values ±1 sigma predicted by the Akkar and Bommer (2010), AkB10, model for rock sites class and $M_w$ 6.9.

analysis to intermediate and high-frequency ranges and summarize the results estimating the median ground-motion values and the standard deviations associated with the parametric uncertainties of the model.

We constructed a large set of possible rupture models for various positions of the rupture nucleation point, final slip distributions on the fault, and rupture velocity values. The first set of scenario rupture models uses the same distribution of slip (Fig. 2a) and rupture velocity ($0.8V_S$) as for the simulation of the 1980 earthquake records; however, we considered six additional hypocenter locations spanning the length of the fault at a depth of about 11 km (Table 2). Further sets of rupture models were generated considering two alternative slip distributions with the same average slip value and different position of asperities (Fig. 2) and two alternative values of rupture velocities ($0.7V_S$ and $0.85V_S$). The two additional slip models are characterized by asperities located on the central portion and on the northwestern portion of the fault, respectively. Note that the same suite of hypocenters and rupture velocities is used for each slip distribution.

For each kinematic rupture model we simulated the time series considering the same receivers grid of Figure 1 and using HIC, EXSIM, and $DSM_{app}$ techniques. Note that we did

not include the $DSM_{fix}$ method as we have shown that it practically provides very similar results to EXSIM. In total, for each technique a data set composed of about 4500 accelerograms was produced, obtained by the combination of 54 rupture models and 84 virtual observers radially distributed within 50 km of the fault. The distribution of simulated PGA and PGV from all the considered rupture models, as a function of $R_{JB}$, is presented in Figure 8.

We compared simulated peak ground motions in terms of median estimates and related variability. We calibrated a simple functional form for the three synthetic data sets, using a similar approach as in empirical GMPEs. Here, no dependence on magnitude, anelastic attenuation term, and focal mechanism are introduced as magnitude and focal mechanism are fixed parameters in the simulations ($M_w$ 6.9, normal fault), and the distance range is within 50 km.

A regression scheme based on the random effect model (Brillinger and Preisler 1985; Abrahamson and Youngs 1992) was adopted in order to decompose the total variability into its components (Strasser *et al.*, 2009; Atik *et al.*, 2010). To keep the terminology clear, we will refer to interscenario (i.e., between-scenario) and intrascenario (i.e., within-scenario) variability (instead of interevent and intraevent variability), because we are not dealing with different events, strictly speaking.

The regressions were performed for the geometric mean of the north–south and east–west components of peak ground motions. The assumed functional form is given by

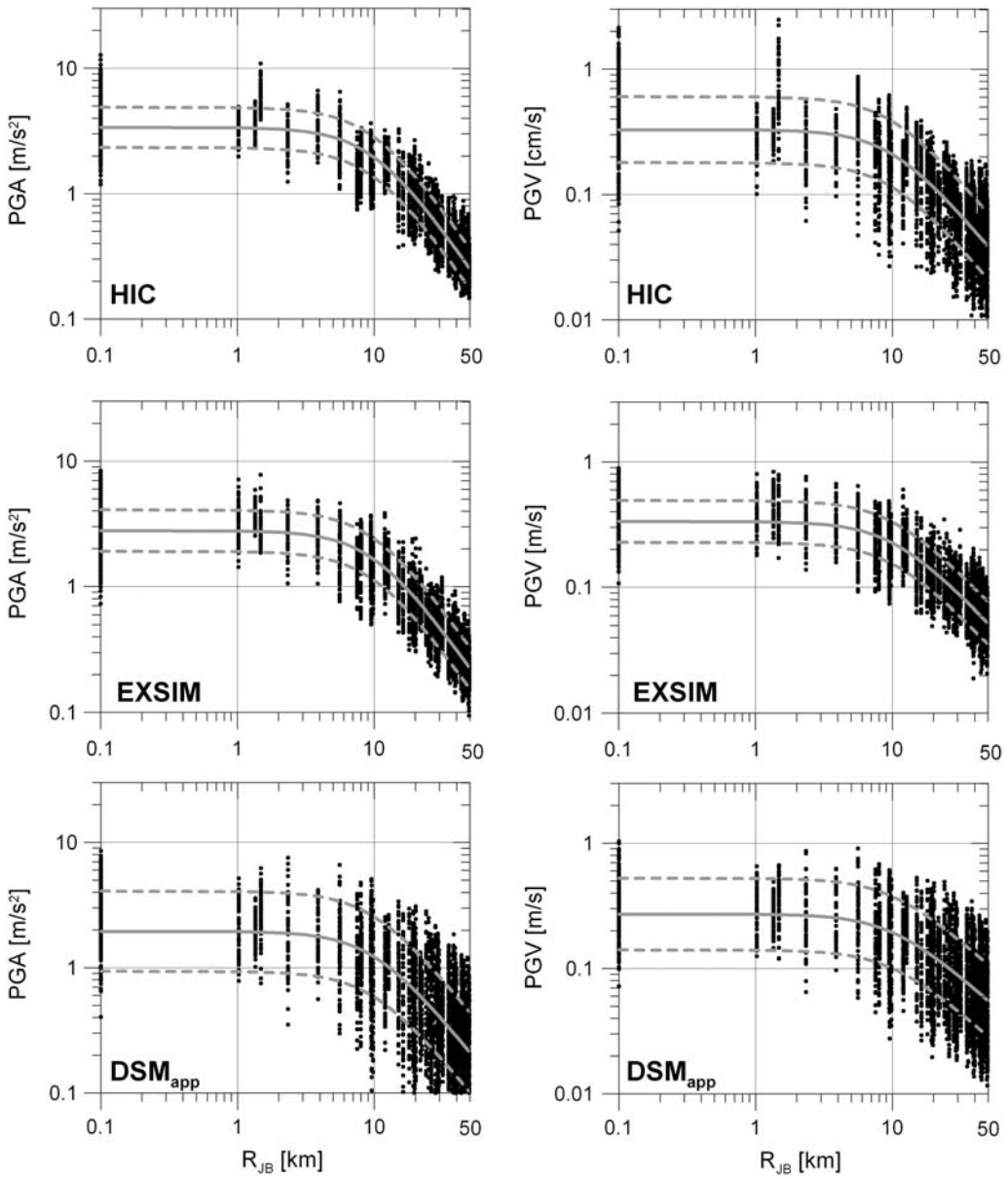


**Figure 8.** PGA and PGV (geometric mean of NS and EW components) from all earthquake scenarios (black symbols) versus $R_{JB}$ distance. Median PGA and PGV $\pm\sigma_{TOT}$ estimated by equations (1) and (2) are shown by gray curves for HIC, EXSIM, and $DSM_{app}$ simulations.

$$\log_{10} Y = a + c \log_{10} \sqrt{(R_{JB}^2 + h^2)} + \delta_{K,i} + \delta_{A,ij}, \quad (1)$$

where $Y$ is the response variable (i.e., PGA or PGV); $h = 10.9$ km (the depth of the hypocenter in the source model), $a$ and $c$ are the coefficients of the regression, and $\delta_{K,i}$ and $\delta_{A,ij}$ represent the interscenario (depending on scenario event $i$ only) and intrascenario (depending both on scenario event $i$ and site $j$) residuals, assumed to be normally distributed with variances $\sigma_K^2$ and $\sigma_A^2$, respectively. The variability of median ground motions predicted for the various scenario events and the variability of ground motions with respect to the median motion predicted for each individual scenario event are represented by $\sigma_K^2$ and $\sigma_A^2$.

The total variance of model (1) is given by

$$\sigma_{TOT}^2 = \sigma_K^2 + \sigma_A^2. \quad (2)$$

Table 5 lists the regression coefficients and sigma values. Figure 8 shows the median curves $\pm\, \sigma_{TOT}$ estimated from equations (1) and (2), considering PGA and PGV calculated for the three data sets. The median ground-motion values of the three simulation methods are consistent, while the relative standard deviations show significant differences, also depending on the considered strong-motion parameter (see Table 5).

The observed difference in the total sigma values implies that $DSM_{app}$ synthetics present the largest PGA variability, whereas only half of such variability is found for EXSIM and HIC peak accelerations. On the other hand, comparable PGV variabilities are found for HIC and $DSM_{app}$, while smaller variability is observed from the EXSIM simulations. The interscenario ($\sigma_K$) and intrascenario ($\sigma_A$) variabilities reveal that the larger contribution to the total sigma comes from the latter (i.e., spatial) variability. Moreover, it can be noticed that the interscenario standard deviations present the lowest values for EXSIM synthetics, whereas $DSM_{app}$ and HIC peaks are characterized by similar $\sigma_K$, though HIC interscenario variability substantially increases for PGVs. These differences in $\sigma_K$ values signify that the influence of the parametric uncertainties on ground-motion estimates is different for each technique. EXSIM method results loosely sensitive to variations in the kinematic rupture model. Conversely, in $DSM_{app}$, the calculation of isochrones and of the use of the apparent corner frequency, implies that the choice of the nucleation point position and of the value of rupture velocity has a large influence on the simulated ground motion. Finally, HIC synthetics, characterized by the largest interscenario variability, are calculated solving the representation theorem at low frequency. As PGV is sensitive to the intermediate frequency of the motion (where the deterministic and stochastic approaches are merged), we expect to observe a larger dependence on the source parameters (e.g., hypocenter location and slip distribution) than for stochastic methods.

## Comparison with GMPEs

In Figure 9a the median PGA and PGV curves from simulated data sets are compared with the median $\pm 1\sigma$ of the AkB10 empirical GMPEs (AkB10 for $M_w = 6.9$) for the rock site class.

The synthetic PGA and PGV median curves are enclosed in the empirical standard deviation, but simulated PGAs exhibit a different decay with distance, attenuating faster for $R_{JB}$ larger than 10 km. This feature, already observed in Figure 7, is common to the all examined rupture scenarios and cannot be considered a peculiarity of the 1980 Irpinia earthquake.

Regarding the synthetics variability (Table 5), the DSM and HIC total standard deviations for PGV are consistent with the AkB10 standard deviation. Conversely, the total synthetic sigma for PGA is similar to the empirical one only for $DSM_{app}$, while it is significantly smaller for the other two simulation techniques.

The median PGA and PGV $\pm$ interscenario ($\sigma_k$) and intrascenario ($\sigma_A$) for HIC are compared with the AkB10 predictions, considering the interevent and intraevent standard deviations separately (Fig. 9b,c). Synthetic interscenario and empirical interevent standard deviations have very similar values both for PGA and PGV, suggesting that the observed ground-motion variability associated with event-specific factors that we have not taken into account (e.g., stress drop, focal depth, etc.) is of the same order of magnitude as the variability caused by different rupture scenarios on the given fault.

Table 5
Regression Coefficients for Equations (1) and (2) for Each of the Adopted Simulation Techniques*

| | PGA | | | | PGV | | | |
|---|---|---|---|---|---|---|---|---|
| | $DSM_{app}$ | EXSIM | HIC | AkB10† | $DSM_{app}$ | EXSIM | HIC | AkB10† |
| $a$ | 3.657 | 3.987 | 4.121 | | 2.407 | 2.666 | 2.831 | |
| $c$ | −1.366 | −1.541 | −1.592 | | −0.974 | −1.141 | −1.314 | |
| $\sigma_K$ | 0.101 | 0.052 | 0.095 | 0.0994 | 0.091 | 0.053 | 0.131 | 0.1083 |
| $\sigma_A$ | 0.303 | 0.157 | 0.129 | 0.2610 | 0.272 | 0.159 | 0.228 | 0.2562 |
| $\sigma_{TOT}$ | 0.320 | 0.165 | 0.161 | 0.2790 | 0.287 | 0.167 | 0.263 | 0.2780 |

*Sigma values for the AkB10 model are also reported.
†For the AkB10 model the reported values for $\sigma_K$ and $\sigma_A$ refer to the interevent and intraevent standard deviations.

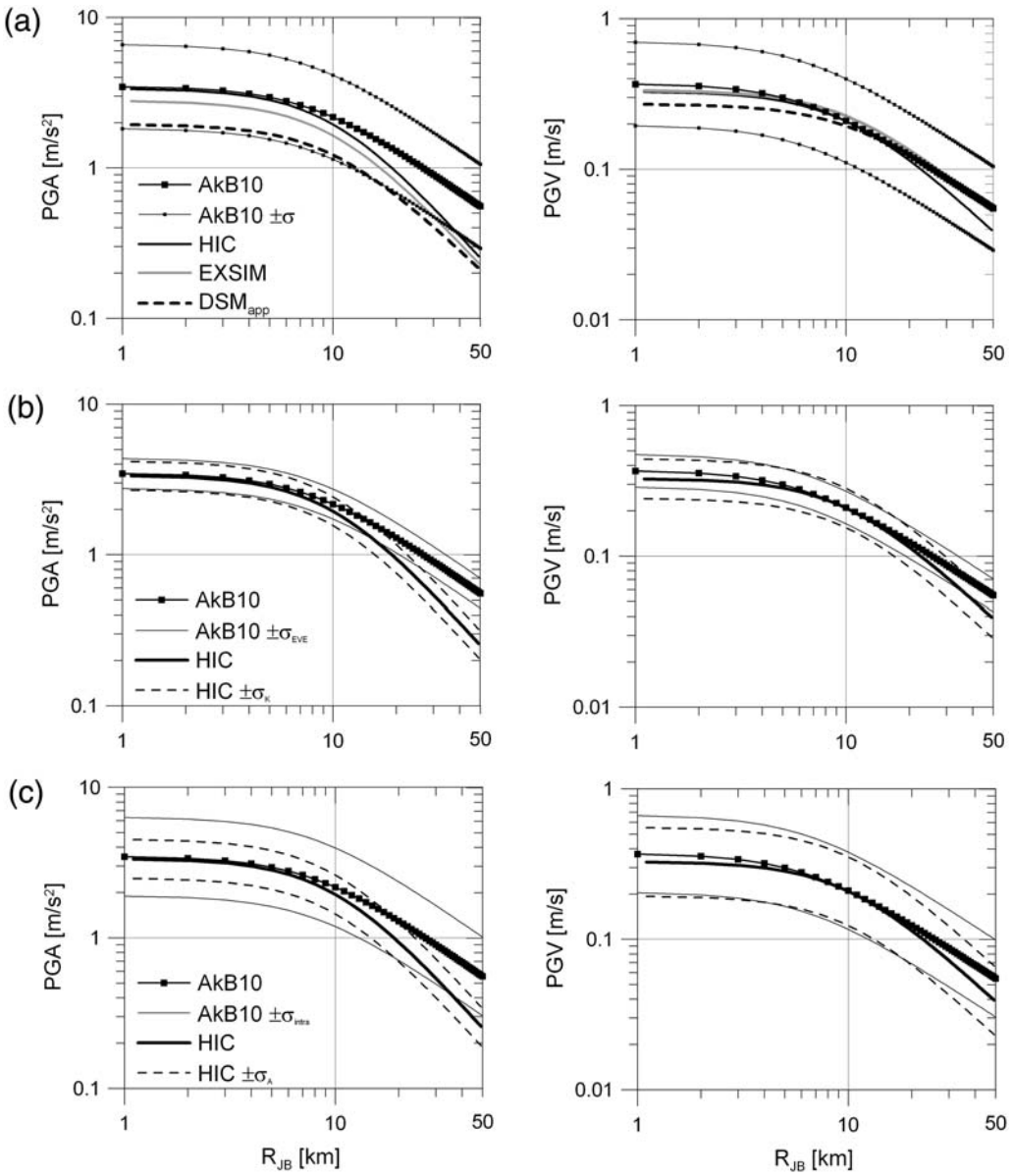


**Figure 9.** (a) Comparison of median PGA and PGV (equation 1) from simulations ($DSM_{app}$, EXSIM and HIC techniques) and Akkar and Bommer (2010), AkB10, GMPEs for rock site class and $M_w$ 6.9. (b) Comparison of PGA and PGV median $\pm 1$ interscenario sigma ($\sigma_k$) from simulations (HIC method only) and AkB10 median $\pm 1$ interevent sigma. (c) Comparison of PGA and PGV median $\pm 1$ intrascenario sigma ($\sigma_A$) from simulations (HIC method only) and AkB10 median $\pm 1$ intraevent sigma.

In Figure 9c we observe that the synthetic intrascenario standard deviation is similar to the empirical one for PGV (right panel) and lower for PGA (left panel). This result means that, at low- to intermediate-frequencies (affecting the PGV), the observed ground-motion spatial variability, including effects depending on record-specific factors (e.g., directivity effects, different response for rock sites, etc.) is of the same order of magnitude as the synthetic one. The synthetic intrascenario variability account for directivity effects, radiation pattern, and source-sites geometry, but the site condition is equal for all sites. Thus, the larger values of PGA empirical intraevent standard deviation as compared with the synthetic one may be explained both by the lack of directivity effects at high frequencies in the synthetics and/or by the randomness in site response for rock sites that can make an important contribution in the observed high-frequency ground-motion variability.

Finally, we observe that $DSM_{app}$ provides a PGA intrascenario variability larger than the AkB10 one (Table 5). This can be ascribed to the overestimation of the spatial variability related to directivity effects as shown in Figure 7.

## Conclusions

In this paper we performed a simulation study for the 1980 $M$ 6.9 Irpinia (southern Italy) earthquake. This seismic event is the largest recorded by strong-motion instruments in Italy, and it involved three distinct shocks. We focused our

attention on the 0 s event, which ruptured the largest fault segment.

The modeling of this event was performed with three finite-fault simulation methods, that is, the finite-fault stochastic method (EXSIM, Motazedian and Atkinson, 2005; Boore, 2009), the hybrid deterministic-stochastic method (DSM, Pacor *et al.*, 2005), and the broadband integral-composite approach (HIC, Gallovič and Brokešová, 2007), assuming the geometry and source kinematic models based on Bernard and Zollo (1989) and Cocco and Pacor (1993). To validate the model parameters, we first calculated synthetic seismograms at bedrock, in correspondence to seven strong-motion stations, classified as rock or stiff sites. We found a general consistency among the simulation results in terms of spectral accelerations and peak values, whereas the synthetic waveforms show remarkable differences in duration and phase. The goodness of fit of the modeling was then assessed by evaluating a model bias, based on acceleration response spectra residuals, that resulted within a value of $\pm 0.25$ (in $\log_{10}$ units) around zero for all of the techniques. We verified that the local site response do not have a predominant effect on ground motion at the investigated stations, except at RNR, where we were not able to explain the high-frequency content of the observed waveforms with the adopted source, propagation, and site parameters.

The validated model was used to simulate the ground motion from the 0 s event at a regular grid of virtual receivers in order to study the ground-motion features at the regional scale. Because of the particular position of the hypocenter, we found peak distributions elongated approximately in the fault-strike direction. HIC and $DSM_{app}$ techniques predicted larger PGV values toward the northwest as an effect of rupture directivity both along the strike and up-dip directions.

The second part of this study concerned the simulation of ground motions from scenario events associated with the 0 s seismogenic fault. We considered 54 different rupture models combining three slip distributions, three rupture velocities, and six positions of the hypocenter. We calculated the synthetic accelerograms, produced by each of the rupture processes, at a grid of 84 virtual receivers radially distributed within 50 km around the fault, with three simulation techniques. In this way, we constructed a data set of more than 4500 synthetic seismograms for each technique, suitable for statistical analyses. We used each synthetic data set to calibrate a simple functional form in order to describe the attenuation with distance of simulated motions from many rupture scenarios in terms of median PGA and PGV and related variability. From the regression analysis we found that the median curves of simulated ground motions are consistent, even if the simulation techniques describe in different ways the source and the wave-propagation processes. On the other hand, the total variability differs from one technique to another. This means that the effect of the parametric uncertainties of simulated ground motions depend on the simulation method.

We compared the synthetic predictions with the empirical GMPEs, and we found that the PGA synthetic median curves are smaller and exhibit a faster decay with distance than the GMPEs. Because the attenuation model used in the simulations have been validated with the data recorded during the 1980 Irpinia earthquake, we conclude that the considered empirical GMPEs for PGA may be too conservative in the case of occurrences of the assumed scenario events.

We also compare the empirical and synthetic standard deviations. Note that, formally, the two quantities describe different components of the total variability in ground-motion prediction: the modeling variability (for empirical GMPEs) and the parametric variability (for simulations) (see Toro *et al.*, 1997). When comparing ground motions variability from GMPEs and synthetics from scenario events, we have to consider that, on the one hand, the constructed scenarios account for the uncertainties of a few source parameters, while other sources of variability (e.g., differences in focal mechanism, site conditions, etc.) considered in GMPEs are fixed in the simulations. On the other hand, the synthetic motions are computed on a much denser distribution of sites around the fault with respect to what is observed in real earthquakes. In this respect, simulations account for a more complete characterization of the spatial distribution of near-fault ground motions. Moreover, it is possible to evaluate the ground-motion variability from different ruptures on the same fault, while, due to the actual lack of such episodes, this variability is missing in GMPEs.

The interscenario ($\sigma_K$) and intrascenario ($\sigma_A$) variabilities reveal that the larger contribution to the total sigma comes from the latter (i.e., spatial variability). The EXSIM synthetics are characterized by the smallest interscenario variability, while the HIC ones are characterized by the largest variability (especially for PGV) due to the deterministic calculations of the motion at low frequencies. The $DSM_{app}$ synthetics present the largest intrascenario variability, which means that, on average, the simulations produce the largest spatial variability of ground motion. This is consistent with the large sensitivity of the $DSM_{app}$ method to the position of the nucleation point that directly affects the rupture directivity (Ameri *et al.*, 2009), producing large spatial variation of ground motion around the fault. High-frequency directivity effects have been observed on strong-motion records from recent moderate-magnitude earthquakes: the 1997 $M$ 5.6–6.0 Umbria–Marche events (Castro *et al.*, 2001; Castro *et al.*, 2008; Emolo *et al.*, 2008) and the 2009 $M$ 6.3 L'Aquila earthquake (Akinci *et al.*, 2010). However, further studies should be carried out to understand if this phenomena could significantly affect the observed ground-motion variability even in this frequency range.

## Data and Resources

Seismograms recorded during the 1980 Irpinia earthquake used in this study, the related ground-motion parameters and stations information can be downloaded from the

Italian Accelerometric Archive (ITACA) at http://itaca.mi.ingv.it (last accessed January 2011).

The EXSIM code has been downloaded from http://www.daveboore.com/software_online.htm (last accessed January 2011).

Some plots were made using the Generic Mapping Tools version 3.3.6 (Wessel and Smith, 1998; http://www.soest.hawaii.edu/gmt/; last accessed January 2008).

## Acknowledgments

This research was funded by DPC–INGV agreement 2004–2007 within the project "S3—Shaking and damage scenarios in area of strategic and/or priority interest" and supported by Grant Agency of the Czech Republic (205/08/P013). We thank the associate editor Hiroshi Kawase, Giovanna Cultrera, and an anonymous reviewer for constructive comments and criticism that greatly improved the quality of the original paper. We thank Gail Atkinson, Dariush Motazedian, and David Boore for providing the EXSIM code. Dino Bindi and Lucia Luzi provided the code for the random effect model.

## References

Aagaard, B. T., T. M. Brocher, D. Dolenc, D. Dreger, R. W. Graves, S. Harmsen, S. Hartzell, S. Larsen, K. McCandless, S. Nilsson, N. A. Petersson, A. Rodgers, B. Sjögreen, and M. L. Zoback (2008). Ground-motion modeling of the 1906 San Francisco earthquake, Part II: Ground-motion estimates for the 1906 earthquake and scenario events, *Bull. Seismol. Soc. Am.* **98,** 1012–1046.

Abrahamson, N. A., and R. R. Youngs (1992). A stable algorithm for regression analyses using the random effects model, *Bull. Seismol. Soc. Am.* **82,** 505–510.

Aki, K., and P. G. Richards (2002). *Quantitative Seismology*, Second Ed. University Science Books, Sausalito, California, 704 pp.

Akinci, A., L. Malagnini, and F. Sabetta (2010). Characteristics of the strong ground motions from the 6 April 2009 L'Aquila earthquake, Italy, *Soil Dyn. Earthquake Eng.* **30,** 320–335.

Akkar, S., and J. J. Bommer (2010). Empirical equations for the prediction of PGA, PGV and spectral accelerations in Europe, the Mediterranean region, and the Middle East, *Seismol. Res. Lett.* **81,** 195–206.

Amato, A., and G. Selvaggi (1993). Aftershock location and *P*-velocity structure in the epicentral region of the 1980 Irpinia earthquake, *Ann. Geophys.* **36,** 3–15.

Ambraseys, N. N., J. Douglas, S. K. Sarma, and P. M. Smit (2005). Equations for the estimation of strong ground motions from shallow crustal earthquakes using data from Europe and Middle East: Horizontal peak ground acceleration and spectral acceleration, *Bull. Earthquake Eng.* **3,** 1–53.

Ameri, G., F. Gallovič, F. Pacor, and A. Emolo (2009). Uncertainties in strong ground-motion prediction with finite-fault synthetic seismograms: An application to the 1984 *M* 5.7 Gubbio, central Italy, earthquake, *Bull. Seismol. Soc. Am.* **99,** 647–663.

Ameri, G., F. Pacor, G. Cultrera, and G. Franceschina (2008). Deterministic ground-motion scenarios for engineering applications: The case of Thessaloniki, Greece, *Bull. Seismol. Soc. Am.* **98,** 1289–1303.

Anderson, J. G., and S. E. Hough (1984). A model for the shape of the Fourier amplitude spectrum of acceleration at high frequencies, *Bull. Seismol. Soc. Am.* **74,** 1969–1993.

Ansal, A., A. Akinci, G. Cultrera, M. Erdik, V. Pessina, G. Tonuk, and G. Ameri (2008). Loss estimation in Istanbul based on deterministic earthquake scenarios of the Marmara Sea region (Turkey), *Soil Dyn. Earth. Eng.* **29,** 699–709.

Archuleta, R. J., and S. H. Hartzell (1981). Effects of fault finiteness on near-source ground motion, *Bull. Seismol. Soc. Am.* **71,** 939–957.

Atik, L. A., N. Abrahamson, J. J. Bommer, F. Scherbaum, F. Cotton, and N. Kuehn (2010). The variability of ground-motion prediction models and its components, *Seismol. Res. Lett.* **81,** no. 5, 794–801.

Atkinson, G. M., and D. M. Boore (2006). Earthquake ground-motion prediction equations for eastern North America, *Bull. Seismol. Soc. Am.* **96,** 2181–2205.

Bernard, P., and R. Madariaga (1984). A new asymptotic method for the modeling of near-field accelerograms, *Bull. Seismol. Soc. Am.* **74,** 539–558.

Bernard, P., and A. Zollo (1989). The Irpinia (Italy) 1980 earthquake: Detailed analysis of a complex normal faulting, *J. Geophys. Res.* **94,** 1631–1647.

Bindi, D., R. R. Castro, G. Franceschina, L. Luzi, and F. Pacor (2004). The 1997–1998 Umbria–Marche sequence (central Italy): Source, path and site effects estimated from strong motion data recorded in the epicentral area, *J. Geophys. Res.* **109,** B04312, doi 10.1029/2003JB002857.

Bindi, D., L. Luzi, M. Massa, and F. Pacor (2009). Horizontal and vertical ground motion prediction equations derived from the Italian Accelerometric Archive (ITACA), *Bull. Earthquake Eng.*, doi 10.1007/s10518-009-9130-9.

Boore, D. M. (1983). Stochastic simulation of high-frequency ground motion based on seismological models of the radiated spectra, *Bull. Seismol. Soc. Am.* **73,** 1865–1894.

Boore, D. M. (2003). Simulation of ground motion using the stochastic method, *Pure Appl. Geophys.* **160,** 635–676.

Boore, D. M. (2009). Comparing stochastic point-source and finite-source ground-motion simulations: SMSIM and EXSIM, *Bull. Seismol. Soc. Am.* **99,** 3202–3216.

Boore, D. M., and G. M. Atkinson (2008). Ground-motion prediction equations for the average horizontal component of PGA, PGV, and 5%-damped PSA at spectral periods between 0.01 s and 10.0 s, *Earthquake Spectra* **24,** 99–138.

Boore, D. M., and W. B. Joyner (1997). Site amplifications for generic rock sites, *Bull. Seismol. Soc. Am.* **87,** 327–341.

Bouchon, M. (1981). A simple method to calculate Green's functions for elastic layered media, *Bull. Seismol. Soc. Am.* **71,** 959–971.

Brillinger, D. R., and H. K. Preisler (1985). Further analysis of the Joyner–Boore attenuation data, *Bull. Seismol. Soc. Am.* **75,** 611–614.

Castro, R., R. F. Pacor, G. Franceschina, D. Bindi, C. Zonno, and L. Luzi (2008). Stochastic strong-motion simulation of the $M_w$ 6 Umbria–Marche earthquake of September 1997: Comparison of different approaches, *Bull. of Seismol. Soc Am.* **98,** no. 2, 662–670, doi 10.1785/0120070092.

Castro, R. R., A. Rovelli, M. Cocco, M. Di Bona, and F. Pacor (2001). Stochastic simulation of strong-motion records from the 26 September 1997 ($M_w$ 6), Umbria–Marche (Central Italy) earthquake, *Bull. Seismol. Soc. Am.* **91,** 27–39.

CEN, Comité Européen de Normalisation (2004). Eurocode 8: Design of Structures for Earthquake Resistance—Part 1: General Rules, *Seismic Actions and Rules for Buildings*, Brussels: Comité Européen de Normalisation.

Chiauzzi, L., A. Masi, M. Mucciarelli, M. Vona, F. Pacor, G. Cultrera, F. Gallovič, and A. Emolo (2010). Building damage scenarios based on exploitation of Housner intensity derived from finite faults ground motion simulation, submitted to *Bull. Earthquake Eng.*

Cocco, M., and F. Pacor (1993). The rupture process of the 1980 Irpinia, Italy, earthquake from the inversion of strong motion waveforms, *Tectonophysics* **218,** 157–177.

Convertito, V., A. Emolo, and A. Zollo (2006). Seismic-hazard assessment for a characteristic earthquake scenario: An integrated probabilistic-deterministic method, *Bull. Seismol. Soc. Am.* **96,** 377–391.

Cultrera, G., A. Cirella, E. Spagnuolo, A. Herrero, E. Tinti, and F. Pacor (2010). Variability of kinematic source parameters and its implication on the choice of the design scenario, *Bull. Seismol. Soc. Am.* **100,** 941–953.

Cultrera, G., F. Pacor, G. Franceschina, A. Emolo, and M. Cocco (2009). Directivity effects for moderate-magnitude earthquakes ($M_w$ 5.6–6.0) during the 1997 Umbria–Marche sequence, central Italy, *Tectonophysics* **476,** 110–120.

Emolo, A., G. Cultrera, G. Franceschina, F. Pacor, V. Convertito, M. Cocco, and A. Zollo (2008). Ground motion scenarios for the 1997 Colfiorito, central Italy, earthquake, *Ann. Geophys.* **51,** 509–525.

Gallovič, F., and J. Brokešová (2004). The $k^{-2}$ rupture model parametric study: Example of the 1999 Athens earthquake, *Studia geoph. et geod.* **48,** 589–613.

Gallovič, F., and J. Brokešová (2007). Hybrid *k*-squared source model for strong ground motion simulations: Introduction, *Phys. Earth Planet. In.* **160,** 34–50.

Gallovič, F., and J. Burjánek (2007). High-frequency directivity in strong ground motion modeling methods, *Ann. Geophys.* **50,** 203–211.

Giardini, D. (1993). Teleseismic observation of the November 23 1980, Irpinia earthquake, *Ann. Geophys.* **36,** 17–25.

Graves, R. W., and A. Pitarka (2010). Broadband ground-motion simulation uUsing a hybrid approach, *Bull. Seismol. Soc. Am.* **100,** 2095–2123.

Heaton, T. H. (1990). Evidence for and implications of self healing pulses of slip in earthquake rupture, *Phys. Earth Planet. In.* **64,** 1–20.

Herrero, A., and P. Bernard (1994). A kinematic self-similar rupture process for earthquakes, *Bull. Seismol. Soc. Am.* **84,** 1216–1228.

Improta, L., M. Bonagura, P. Capuano, and G. Iannaccone (2003). An integrated geophysical investigation of the upper crust in the epicentral area of the 1980, $M_s = 6.9$, Irpinia earthquake (Southern Italy), *Tectonophysics* **361,** no. 1–2, 139–169.

Joyner, W. B., and D. M. Boore (1981). Peak horizontal acceleration and velocity from strong-motion records including records from the 1979 Imperial Valley, California, earthquake, *Bull. Seismol. Soc. Am.* **71,** 2011–2038.

Kwon, O., and A. S. Elnashai (2006). The effect of material and ground motion uncertainty on the seismic vulnerability curves of a RC structure, *Engineering Structures* **28,** 289–303.

Lermo, J., and F. J. Chávez-García (1993). Site effect evaluation using spectral ratio with only one station, *Bull. Seismol. Soc. Am.* **83,** 1574–1594.

Luzi, L., S. Hailemikael, D. Bindi, F. Pacor, F. Mele, and F. Sabetta (2008). ITACA (ITalian ACcelerometric Archive): A web portal for the dissemination of Italian strong-motion data, *Seismol. Res. Lett.* **79,** 716–722.

Mai, P. M., and G. C. Beroza (2003). A hybrid method for calculating near-source, broadband seismograms: Application to strong motion prediction, *Phys. Earth Planet. Int.* **137,** 183–199.

Margaris, B. N., and D. M. Boore (1998). Determination of $\Delta\sigma$ and $\kappa_0$ from response spectra of large earthquakes in Greece, *Bull. Seismol. Soc. Am.* **88,** 170–182.

Mena, B., E. Durukal, and M. Erdik (2006). Effectiveness of hybrid Green's function method in the simulation of near field strong motion: An application to the 2004 Parkfield earthquake, *Bull. Seismol. Soc. Am.* **96,** S183–S205.

Motazedian, D., and G. M. Atkinson (2005). Stochastic finite-fault modelling based on a dynamic corner frequency, *Bull. Seismol. Soc. Am.* **95,** 995–1010.

National Earthquake Hazards Reduction Program (1994). FEMA report 222A/223A, Recommended provisions for seismic regulations for new buildings, Provision 1 and Commentary 2, Federal Emergency Management Agency, Washington, D.C.

NTC08, Norme Tecniche per le Costruzioni (2008). DM 140108, Ministero delle Infrastrutture, Roma, Gazzetta Ufficiale, http://www.cslp.it/cslp/index.php?option=com_content&task=view&id=66&Itemid=20 (in Italian). Last accessed January 2011.

Olivares, L., and F. Silvestri (2001). Analisi della risposta sismica e della subsidenza post-sismica del colle di Bisaccia a seguito del terremoto irpino-lucano del 1980, *Proc. X National Conference of ANIDIS* (in Italian).

Pacor, F., G. Cultrera, A. Mendez, and M. Cocco (2005). Finite fault modeling of strong ground motions uing a hybrid deterministic–stochastic approach, *Bull. Seismol. Soc. Am.* **95,** 225–240.

Pantosti, D., and G. Valensise (1990). Faulting mechanism and complexity of the 23 November 1980, Campania–Lucania earthquake, inferred from surface observations, *J. Geophys. Res.* **95,** 15319–15341.

Pingue, F., G. De Natale, and P. Briole (1993). Modeling of the 1980 Irpinia earthquake source : Constrains from geodetic data, *Ann. Geophys.* **36,** 27–40.

Ripperger, J., P. M. Mai, and J. P. Ampuero (2008). Variability of near-field ground motion from dynamic earthquake rupture simulations, *Bull. Seismol. Soc. Am.* **92,** 2217–2232.

S3 Project Deliverable D0 (2007). Scenari di scuotimento in aree di interesse prioritario e/o strategico, Deliverable D0: Tecniche di simulazione. http://esse3.mi.ingv.it/deliverables/Deliverables_D0_S3_last.pdf (in Italian). Last accessed January 2011.

Siddiqqi, J., and G. Atkinson (2002). Ground motion amplification at rock sites across Canada, as determined from the horizontal-to-vertical component ratio, *Bull. Seismol. Soc. Am.* **92,** 877–884.

Sørensen, M. B., N. Pulido, and K. Atakan (2007). Sensitivity of ground-motion simulations to earthquake source parameters: A case study for Istanbul, Turkey, *Bull. Seismol. Soc. Am.* **97,** 881–900.

Spudich, P., and L. N. Frazer (1984). Use of ray theory to calculate high-frequency radiation from earthquake sources having spatially variable rupture velocity and stress drop, *Bull. Seismol. Soc. Am.* **74,** 2061–2082.

Strasser, F. O., N. A. Abrahamson, and J. J. Bommer (2009). Sigma: Issues, insights, and challenges, *Seismol. Res. Lett.* **80,** 41–56.

Toro, G. R., N. A. Abrahamson, and J. F. Schneider (1997). Model of strong ground motions from earthquakes in Central and Eastern North America: Best estimates and uncertainties, *Seismol. Res. Lett.* **68,** no. 1, 41–57.

Wessel, P., and W. H. F. Smith (1998). New, improved version of the Generic Mapping Tools released, *Eos Trans. AGU* **79,** 579.

Zeng, Y., J. G. Anderson, and G. Y. Anderson (1994). A composite source model for computing realistic synthetic strong ground motions, *Geophys. Res. Lett.* **21,** 725–728.

Zhu, T. J., A. C. Heidebrecht, and W. K. Tso (1988). Effect of peak ground acceleration to velocity ratio on ductility demand of inelastic systems, *Earthq. Eng. Struct. Dyn.* **16,** 63–79.

Zollo, A., A. Bobbio, A. Emolo, A. Herrero, and G. De Natale (1997). Modelling of ground acceleration in the near source range: The case of 1976, Friuli earthquake ($M = 6.5$), northern Italy, *J. Seismol.* **1,** 305–319.

Istituto Nazionale di Geofisica e Vulcanologia
Sezione di Milano-Pavia, Via Bassini, 15
20133, Milano, Italy
ameri@mi.ingv.it
(G.A., F.P.)

Dipartimento di Scienze Fisiche
Università degli Studi "Federico II"
Napoli, Italy
(A.E.)

Charles UniversityFaculty of Mathematics and Physics, Dept. of Geophysics
V Holesovickach 2, Praha 8
180 00, Czech Republic
(F.G.)

Manuscript received 25 August 2010